Impedance measurements and modeling of a transition-edge-sensor calorimeter

Mark A. Lindeman[a] and Simon Bandler
NASA Goddard Space Flight Center, Greenbelt, Maryland 20771 and Department of Astronomy, University of Maryland, College Park, Maryland 20742

Regis P. Brekosky
NASA Goddard Space Flight Center, Greenbelt, Maryland 20771 and Swales Aerospace, Beltsville, Maryland 20705

James A. Chervenak and Enectali Figueroa-Feliciano
NASA Goddard Space Flight Center, Greenbelt, Maryland 20771

Fred M. Finkbeiner
NASA Goddard Space Flight Center, Greenbelt, Maryland 20771 and Science, System and Application, Inc., Lanham, Maryland 20706

Mary J. Li and Caroline A. Kilbourne
NASA Goddard Space Flight Center, Greenbelt, Maryland 20771

(Received 23 June 2003; accepted 9 February 2004; published 26 April 2004)

We describe a method for measuring the complex impedance of transition-edge-sensor (TES) calorimeters. Using this technique, we measured the impedance of a Mo/Au superconducting transition-edge-sensor calorimeter. The impedance data are in good agreement with our linear calorimeter model. From these measurements, we obtained measurements of unprecedented accuracy of the heat capacity and the gradient of resistance with respect to temperature and current of a TES calorimeter throughout the phase transition. The measurements probe the internal state of the superconductor in the phase transition and are useful for characterizing the calorimeter. [DOI: 10.1063/1.1711144]

I. INTRODUCTION

We are developing superconducting transition-edge sensor (TES) calorimeters for x-ray astronomy.[1] Each of our transition edge sensors is a square Mo/Au bilayer film, with a resistance of approximately 10 mΩ. Through the proximity effect, the Mo and the Au act as one superconductor, with the critical temperature T_c determined by the thicknesses of the layers.[2] We design our TES to have critical temperature of approximately 100 mK. The TES is suspended by a silicon nitride membrane to thermally decouple it from the silicon substrate on which the devices are fabricated.[3] In the phase transition between the superconducting and normal metal states, the electrical resistance of the TES increases rapidly with increasing temperature. The TES functions as a very sensitive thermometer in the x-ray calorimeter. It measures small changes in temperature caused by the absorption of single x-ray photons. Our TES calorimeters have demonstrated excellent energy resolutions:[4,5] 2.4 eV at 1.5 keV and 3.7 eV at 3.3 keV.

In operation, the temperature of the substrate is cooled below T_c and a dc voltage bias is applied to the TES. The electrical current through the TES is measured by a dc superconduction quantum interference device (SQUID) array.[6,7] Negative electrothermal feedback in the calorimeter shortens the fall time of the pulses[8,9] and keeps the temperature of the TES near T_c.

We present a linear model of our TES calorimeter, which describes the noise and the response to photons. We fit this calorimeter model to the impedance data to find the heat capacity of the calorimeter, the logarithmic derivatives of the TES resistance with respect to temperature and current, and the inductance in the circuit which biases the TES. We measure the impedance by recording the response of the calorimeter to noise that we add to the bias of the TES. We find that our linear model accurately represents the impedance data.

Our TES impedance data yield precise measurements of the heat capacity and the gradient of the resistance with respect to current and temperature throughout the superconducting phase transition. These measurements are useful for probing the internal state of the TES in the transition.

II. MODELING

Our TES calorimeter model describes the response of the calorimeter to signal and noise. This model includes the two circuits illustrated in Fig. 1. The electrical circuit includes the Thevenin equivalent bias voltage V_{Th}, the electrical current I_{TES}, the TES resistance R, the Thevenin equivalent resistance R_{Th}, and inductance L. The Thevenin equivalent resistance represents the combined contributions of all the resistors of the physical bias circuit in Fig. 2. The thermal circuit includes the heat capacity C of the TES calorimeter,

[a]Electronic mail: Mark.A.Lindeman.1@gsfc.nasa.gov

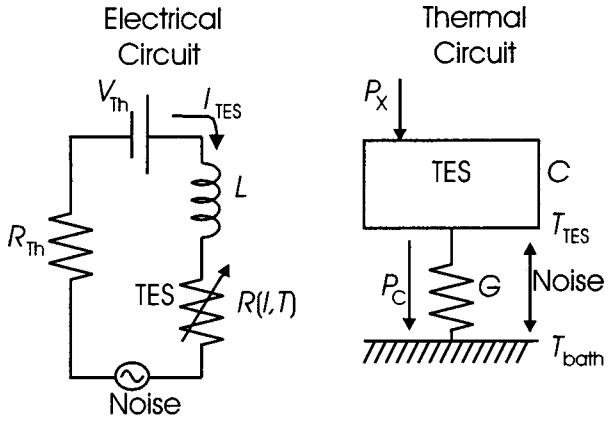

FIG. 1. The TES calorimeter model. The model consists of an electrical circuit and a thermal circuit, which together model the dynamics of a simple TES calorimeter. Noise sources in the electrical circuit are represented by a fluctuating voltage in series with the TES. Noise sources in the thermal circuit are represented by a fluctuating power between the TES and the bath.

the heat flow power P_C from the calorimeter to the substrate, the power into the TES from absorption of radiation P_X, the effective temperature T_{TES} of the TES, and the temperature of the substrate T_{bath}. Note that the resistance of the TES depends on both the current I_{TES} and temperature T_{TES}. In addition, there are sources of noise: phonon noise P_{PN} between the TES and the substrate, Johnson noise of the electronics V_{EN}, the TES electronic noise V_{TN} (which includes

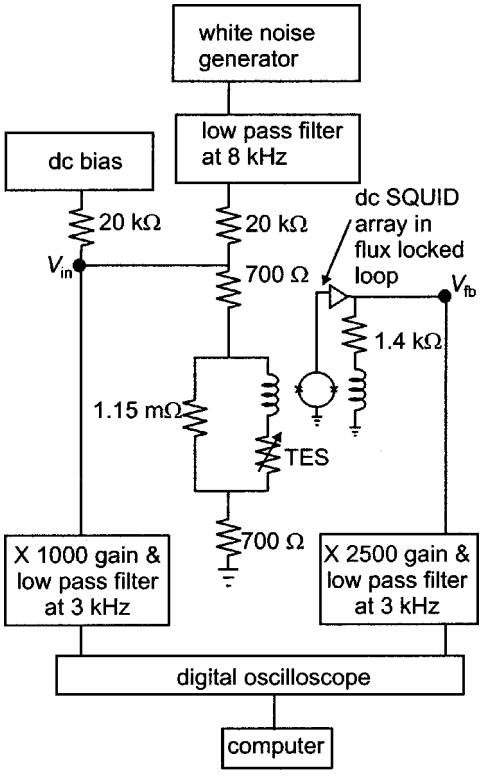

FIG. 2. The electronic setup for the impedance measurements. The digital scope is used to measure the voltage noise put into the bias and the resulting current noise near the TES (with some amplification and filtering). The noise in the bias voltage V_{in} is proportional to the voltage noise V_{BN} near the TES. The flux-locked dc SQUID feedback voltage V_{FB} is proportional to the current I through the TES. The impedance is computed from the Fourier transforms of V_{BN} and I.

Johnson noise plus excess electronic noise in the TES), and the bias noise V_{BN}. The two circuits with noise included are described by the following differential equations:

$$L\frac{dI_{\mathrm{TES}}}{dt}=V_{\mathrm{Th}}-(I_{\mathrm{TES}}R_{\mathrm{Th}}+I_{\mathrm{TES}}R+V_{\mathrm{TN}}+V_{\mathrm{EN}}+V_{\mathrm{BN}}),$$

$$C\frac{dT_{\mathrm{TES}}}{dt}=I_{\mathrm{TES}}^2R-P_C+P_X+I_{\mathrm{TES}}V_{\mathrm{TN}}+P_{\mathrm{PN}}. \tag{1}$$

Note that the V_{TN} noise term appears in both differential equations. In our TES calorimeters, the effect of the Johnson noise and excess TES noise on the current is significantly reduced at frequencies within the bandwidth of the calorimeter because the two terms containing V_{TN} partially cancel out.[8,10,11]

By making the small signal approximation by linearizing Eqs. (1) around equilibrium and retaining terms that are first order with respect to the variables, which include current, temperature, power P_X, and the noise sources, the linear model can be written as

$$\frac{d}{dt}\begin{pmatrix} I \\ T \end{pmatrix}=\begin{pmatrix} -\dfrac{R_{\mathrm{Th}}+R_0+I_0(\partial R/\partial I)}{L} & -\dfrac{I_0}{L}\dfrac{\partial R}{\partial T} \\ \dfrac{I_0R_0}{C}\left(2+\dfrac{I_0}{R_0}\dfrac{\partial R}{\partial I}\right) & \dfrac{I_0^2}{C}\dfrac{\partial R}{\partial T}-\dfrac{G}{C} \end{pmatrix}\begin{pmatrix} I \\ T \end{pmatrix} + \begin{pmatrix} -(V_{\mathrm{TN}}+V_{\mathrm{EN}}+V_{\mathrm{BN}})/L \\ (I_0V_{\mathrm{TN}}+P_{\mathrm{PN}}+P_X)/C \end{pmatrix}, \tag{2}$$

where I_0, T_0, are R_0 are the equilibrium current, temperature and resistance.[11,12] We let $I=I_{\mathrm{TES}}-I_0$ and $T=T_{\mathrm{TES}}-T_0$. The thermal conductance across the membrane is $G=\partial P_C/\partial T$. First-order terms containing $\partial C/\partial T$ and $\partial C/\partial I$ do not appear in Eq. (2) because they cancel out.

The pulse shape can be calculated from the eigenvalues and eigenvectors of the matrix in Eq. (2). If the inductance L is too large, the TES calorimeter may be under damped or unstable, which occurs when the eigenvalues are non-negative.[11]

In this linear approximation, the TES resistance is approximated by

$$R=R_0(1+\alpha_1T/T_0+\beta_1I/I_0), \tag{3}$$

where $\alpha_I=(T_0/R_0)(\partial R/\partial T)$ with I held constant and $\beta_I=(I_0/R_0)(\partial R/\partial I)$ with T held constant.[11] This expression of the TES resistance is obtained by collecting the terms in Eq. (2) that represent the resistance of the TES in the electrical circuit. The value of α_I greatly affects the energy resolution of the calorimeter and the decay time of the pulses.[8,11,13] The value of β_I modifies the impedance of the calorimeter at high frequencies. (Note the terms α_I and β_I have been previously referred to as α and β in other publications. However we include the subscripts in α_I and β_I to distinguish these terms from similar terms with different partial derivatives. The subscript "I" refers to the fact that the partial derivatives are taken with respect to current I and temperature, not voltage and temperature.)

III. DERIVATION OF CALORIMETER RESPONSE AND COMPLEX IMPEDANCE

We take the Fourier transform of Eq. (2) to find the response of the TES calorimeter to signal and noise as a function of frequency f:

$$\mathbf{M}\begin{pmatrix} I \\ T \end{pmatrix} = \begin{pmatrix} -(V_{\mathrm{TN}}+V_{\mathrm{EN}}+V_{\mathrm{BN}})/L \\ (I_0 V_{\mathrm{TN}}+P_{\mathrm{PN}}+P_X)/C \end{pmatrix}, \tag{4}$$

where the matrix in Eq. (4) is

$$\mathbf{M} = \begin{pmatrix} i(2\pi f)+\dfrac{R_{\mathrm{Th}}+R_0+I_0(\partial R/\partial I)}{L} & \dfrac{I_0}{L}\dfrac{\partial R}{\partial T} \\ -\dfrac{I_0 R_0}{C}\left(2+\dfrac{I_0}{R_0}\dfrac{\partial R}{\partial I}\right) & i(2\pi f)-\left(\dfrac{I_0^2}{C}\dfrac{\partial R}{\partial T}-\dfrac{G}{C}\right) \end{pmatrix}. \tag{5}$$

The solution of Eq. (4) is

$$\begin{pmatrix} I \\ T \end{pmatrix} = \mathbf{M}^{-1}\begin{pmatrix} -(V_{\mathrm{TN}}+V_{\mathrm{EN}}+V_{\mathrm{BN}})/L \\ (I_0 V_{\mathrm{TN}}+P_{\mathrm{PN}}+P_X)/C \end{pmatrix}. \tag{6}$$

The current, temperature, and noise terms are all functions of frequency f. Equation (6) describes the frequency dependent response of the microcalorimeter to signal and noise. The noise equivalent power (NEP) of each of the noise sources is calculated by referring the noise to an equivalent noise in the power P_X. The noise limited energy resolution (or baseline energy resolution) of the calorimeter is calculated from the NEP.[13] This method of modeling and solving for signal and noise in calorimeters (referred to as the matrix method) is easily extended to more complicated calorimeters and bolometers.[11,14]

We measure the total impedance in the electrical circuit by putting white noise into the bias. We measure the bias noise V_{BN} and the current I through the TES. We neglect the noise sources except for V_{BN}, and solve Eq. (6) for the impedance $Z=V_{\mathrm{BN}}/I$. The solution is

$$Z = i(2\pi f)L + R_{\mathrm{Th}} + Z_{\mathrm{TES}}, \tag{7}$$

where

$$Z_{\mathrm{TES}}(f) = R_0\left[(1+\beta_I)+\frac{2+\beta_I}{2}\frac{I_0^2 R_0}{CT}\alpha_I\tau_{\mathrm{eff}} \times\left(-1+\frac{1+i(2\pi f)\tau_{\mathrm{eff}}}{-1+i(2\pi f)\tau_{\mathrm{eff}}}\right)\right] \tag{8}$$

and

$$\tau_{\mathrm{eff}} = \left(\frac{I_0^2 R_0}{CT_0}\alpha_1 - \frac{G}{C}\right)^{-1}. \tag{9}$$

The impedance Z_{TES} traces a semicircle in the complex plane.[10,15] We fit the model impedance Z to measured impedance data to obtain values of α_I, β_I, C, and L.

When we measure the impedance, we apply bias noise V_{BN} large enough so that it dominates over other noise sources such as phonon noise and electronic noise. The other noise sources cause scatter in the measurement of the impedance Z.

IV. EXPERIMENT

In this experiment, we characterized a 600 μm square Mo/Au TES which was suspended on 0.5 μm thick membrane of silicon nitride. The bilayer consisted of 50 nm of Mo and 270 nm of Au. (Critical temperature $T_c=98.5$ mK. Normal state resistance $R_N=9.1$ mΩ.) In preparation for the impedance measurements, we measured a series of current-voltage ($I-V$) characteristics of the TES to obtain values for the parameters G, I_0, R_0, and R_{Th} in the calorimeter model.[3,11] From these measurements, we found the thermal coupling of the calorimeter through the membrane to the substrate ($G=344$ pW/K). We performed the impedance measurements with the refrigerator (and substrate) regulated to $T_{\mathrm{bath}}=91.7$ mK. Current-voltage characteristics were measured at that temperature to obtain the TES current I_0 and resistance R_0 as a function of dc bias voltage.

The TES bias circuit in the refrigerator is depicted in Fig. 2. The Thevenin equivalent voltage V_{Th} is $V_{\mathrm{in}}/(1.21\times10^6)$. The Thevenin resistance R_{Th} is 1.45 mΩ, which includes the 1.15 mΩ shunt resistor in our bias circuit plus 0.30 mΩ of parasitic resistance in series with the TES. The resistance of the shunt resistor was calibrated through a measurement of its Johnson noise.

To perform an impedance measurement, we applied a dc voltage bias plus approximately 1.4 μV/Hz$^{1/2}$ noise to the bias at V_{in}, which corresponds to a bias noise of $V_{\mathrm{BN}}=20$ pV/Hz$^{1/2}$ near the calorimeter. Noise from the white noise generator was low-pass filtered at 8 kHz to minimize the fluctuation in the bias of the TES. The bias noise was larger than other sources of noise at frequencies up to 8 kHz. (For example, the TES noise[5] is several hundred fV/Hz$^{1/2}$.) We used a digital oscilloscope to sample the bias noise V_{BN} and the TES current I. We acquired 400 sweeps of 8192 samples each of the bias and signal for each impedance measurement. The sample rate was 10 000 samples per second. Low pass filters (at 3 kHz) were used to antialias the bias and the current signals. We performed an impedance measurement of the TES at each of the bias points plotted on the IV curve of Fig. 3.

V. DATA ANALYSIS

We begin data reduction by filtering out sweeps in which a pulse is detected in the current of the TES. This is neces-

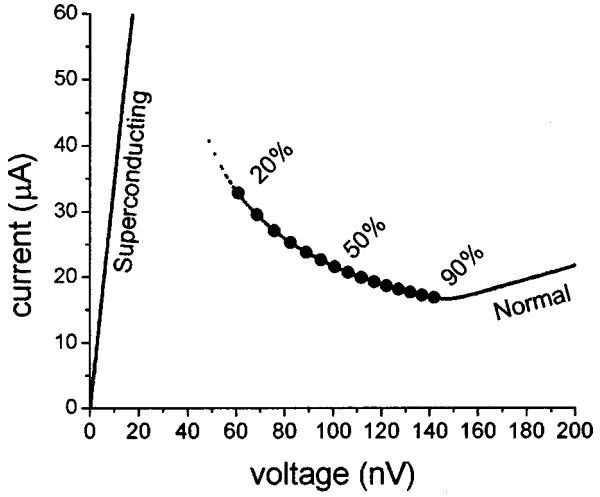

FIG. 3. An $I-V$ curve of the Mo/Au TES and bias points of the impedance measurements. The bias points are in steps of approximately 5% of the normal resistance of the TES. The voltage is applied to the TES plus 300 $\mu\Omega$ of parasitic resistance in series. The substrate temperature is 91.7 mK.

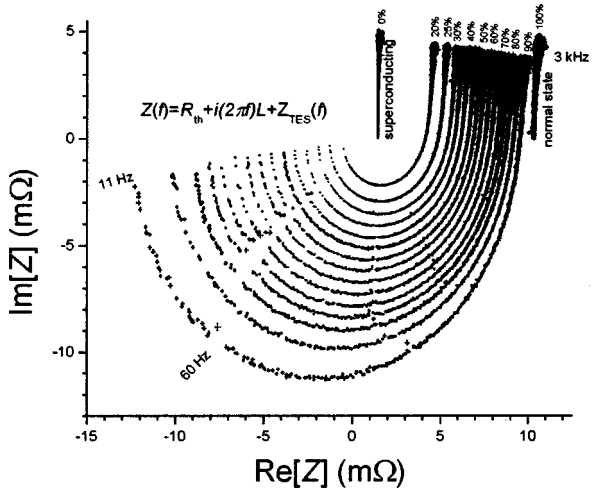

FIG. 4. Measured impedance Z. The small cross around each of the points represents the 1σ error bars. Each trajectory is a measurement of the TES impedance Z_{TES} plus inductance L and resistance R_{Th} in series. The impedance is plotted for frequencies between 11 Hz and 3 kHz. When the TES in the phase transition, its impedance is represented by a semicircle in the complex plane. When the TES is in the normal state or the superconducting state, the impedance is a strait line with $\mathrm{Im}[Z]=2\pi fL$. Data at frequencies with significant radio-frequency interference are excluded.

sary because an x-ray source was positioned near the TES for other experiments. We Fourier transform the remaining data to obtain the bias voltage and TES current as a function of frequency. The impedance is obtained from the following weighted average:

$$Z(f)=\frac{\mathrm{Re}[\Sigma_j x_j y_j^*]+i\,\mathrm{Im}[\Sigma_j x_j^* y_j]}{\Sigma_j |x_j|^2}, \tag{10}$$

where $x_j(f)$ and $y_j(f)$ are, respectively, the jth Fourier transformed measurements of the TES current I, and the bias noise V_{BN}. The weighted average gives a more precise result than simply measuring V_{th}/I. The standard deviation measurements of the real and imaginary parts of Z are

$$\sigma_{\mathrm{Re}}=\frac{\sqrt{\Sigma_j(\mathrm{Re}[x_j]^2\sigma_1^2+\mathrm{Im}[x_j]^2\sigma_2^2)}}{\Sigma_j |x_j|^2} \tag{11}$$

and

$$\sigma_{\mathrm{Im}}=\frac{\sqrt{\Sigma_j(\mathrm{Re}[x_j]^2\sigma_2^2+\mathrm{Im}[x_j]^2\sigma_1^2)}}{\Sigma_j |x_j|^2}, \tag{12}$$

where $\sigma_1(f)$ is the measured standard deviation of $\mathrm{Re}[(y_j - Zx_j)]$ and $\sigma_2(f)$ is the measured standard deviation of $\mathrm{Im}[(y_j - Zx_j)]$. The standard deviations σ_1 and σ_2 represent noise from the TES and bias circuit as referred to voltage V_{Th}. The standard deviation of the real part of Z should equal the standard deviation of the imaginary part because the phase of the noise is random.

After the data processing software obtains the impedance Z from Eq. (10) and the statistical error bars (associated with the noise) from Eqs. (11) and (12), the software rejects data at frequencies where significant electrical pick up is detected. The remaining data between 11 Hz and 3 kHz are plotted in Fig. 4.

In the final step of the data reduction, Eq. (7) is fitted to the impedance data. The temperature T_0 of the TES is approximately equal to T_c. Four parameters, α_I, β_I, C, and L, are the free parameters in the fit of the model to the impedance data.

VI. RESULTS

Figure 5 illustrates a fit of the linear model to an impedance measurement. The linear model fits the impedance data well—especially considering how small are the statistical error bars. The reduced χ^2 of the fit ranges from 1.1 to 1.9 for the impedance measurements plotted in Fig. 4. The greatest difference between the model and data occurs at frequencies less than 100 Hz. This discrepancy is most likely caused by small x-ray pulses, which are not detected or filtered out by

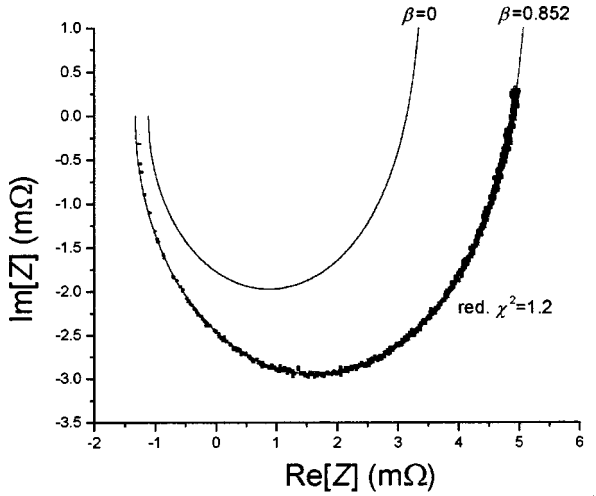

FIG. 5. An example of a model fit to the impedance data and the same model with $\beta_I=0$. We fit the linear model to the impedance data with four free parameters: α_I, β_I, C, and L. The model without β_I cannot fit the impedance data because the impedance of the TES at high frequency strongly depends on β_I.

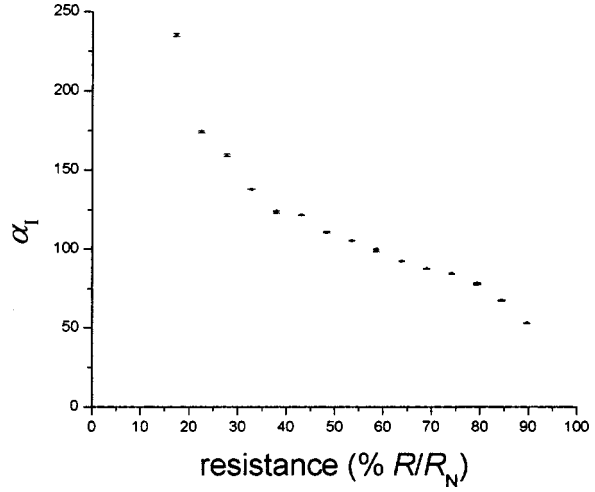

FIG. 6. Impedance measurements of α_I vs TES resistance. (The TES resistance is plotted as a percentage of the normal state resistance of the TES.) Vertical error bars represent the 1σ statistical errors due to noise. Systematic errors are estimated to be $+/-3\%$.

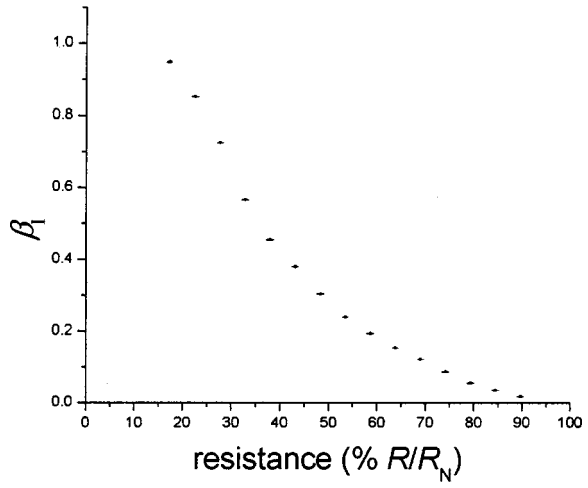

FIG. 7. Impedance measurements of β_I vs TES resistance. Vertical error bars represent the 1σ statistical errors due to noise. Systematic errors are estimated to be $+/-0.01$.

the data software. However, the effect of small pulses on the values of the fitted parameters is relatively small compared to other sources of systematic error.

We obtained precise values of α_I, β_I, C, and L from the impedance measurements. The systematic errors in the measured values of these parameters are much larger than statistical errors, which are caused by noise in the TES and electronics. Systematic errors arise from inaccurate measurement of the model parameters: G, I_0, R_0, R_{Th}, T_0, and from incomplete filtering of small pulses. The dominant source of error is caused by inaccurate measurement of R_0 due to thermal drift during the 3 h it took to perform the impedance measurements. This drift causes the power dissipated by the TES to change by tens of femtowatts. In response, the resistance R_0 of the TES is estimated to drift up to 1 or 1.5%, depending on bias. This drift is estimated to cause an error in the measured heat capacity C up to approximately 4 to 6%, depending on bias. However, repeat measurements of the TES heat capacity at the same bias (separated by several hours) agree to within approximately 1%, indicating that this error may actually be less than we estimated.

The measured values of α_I, β_I, and C are plotted as a function of TES resistance in Figs. 6, 7, and 8. Note that the measured heat capacity of the TES is between the calculated normal-metal heat capacity of the TES and the calculated BCS capacity, as expected. We obtained a value of the inductance ($L=260$ nH) that is consistent with previous measurements of stray inductance in the bias circuit.

We obtained precise measurements of TES resistance R from the $I-V$ curves, and its partial derivatives, $(\partial R/\partial T)$ and $(\partial R/\partial I)$, from the impedance measurements. Using this data, we plot the trajectory of $R(I,T)$ corresponding to the $I-V$ curve of Fig. 3. The $R(I,T)$ data is shown in Fig. 9. By using the partial derivatives, we extrapolate the contours of resistance R in the neighborhood of the trajectory. This data is plotted in Fig. 10. These plots illustrate how the resistance of our Mo/Au TES depends on both temperature and current. Note that we could more completely characterize the surface $R(I,T)$ and the phase transition with additional impedance measurements, taken with different bath temperatures.

VII. DISCUSSION

The heat capacity profile in Fig. 8 is informative with regard to the internal state of the TES in the phase transition. These data indicate that in the middle of the phase transition the TES is not mostly superconducting (for which for we would expect to measure the BCS heat capacity) nor is the TES mostly in the normal state (which would result in the TES having a heat capacity similar to normal state heat capacity). Instead, the heat capacity of our Mo/Au TES gradually increased from the normal state heat capacity toward the BCS heat capacity with decreasing TES resistance. The hy-

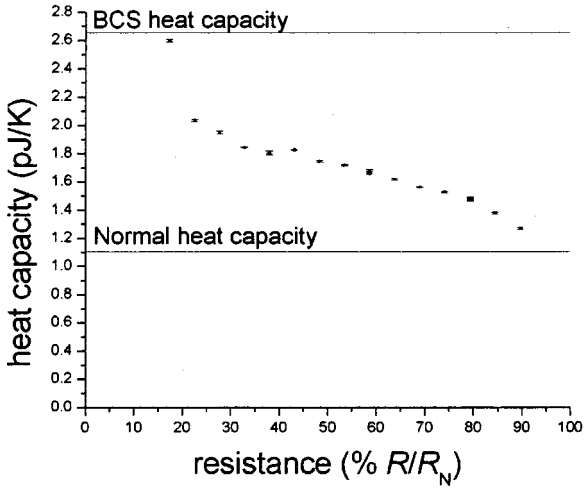

FIG. 8. Impedance measurements of heat capacity vs TES resistance. Vertical error bars represent the 1σ statistical errors due to noise. Systematic errors are estimated to be 4 to 6% depending on the bias point. The measured heat capacity lies between the calculated normal state heat capacity and the BCS heat capacity as expected. This heat capacity profile provides information about the internal state of the TES in the phase transition.

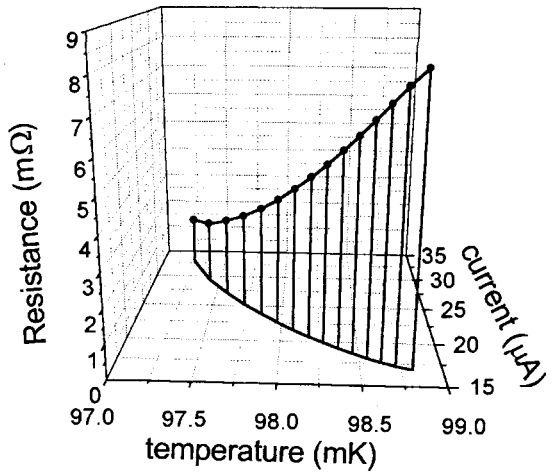

FIG. 9. TES resistance vs current and temperature. This data corresponds to the bias points plotted in Fig. 3.

pothesis that the TES is separating into normal metal and superconducting domains is consistent with this data.

The measured values of α_I, β_I, and C are in good agreement with previous measurements of these parameters of our TESs, which we obtained through other methods such as fitting the model to pulses[12]—but the impedance method is more precise. The heat capacity of a 500 micron square Mo/Au TES (with $T_c = 104$ mK, $R_N = 9.8$ mΩ) is plotted in Fig. 11. These data were obtained by fitting Eq. (6) to pulses resulting from the absorption of Al Kα x rays in the TES. The pulse data also shows that the heat capacity increases from the calculated normal state heat capacity to the BCS heat capacity.

The impedance data are less susceptible to errors due to nonlinearities in the transition than pulse data are. During the impedance measurement, the bias noise V_{BN} is kept relatively small to minimize the perturbations in the TES. The TES remains in the linear small signal regime, and the response can be accurately modeled with Eq. (2).

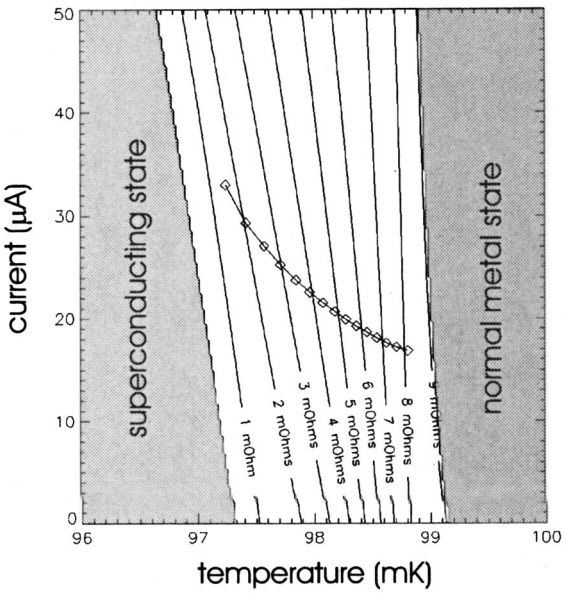

FIG. 10. Extrapolated contours of resistance. The plotted trajectory corresponds to the bias points plotted in Fig. 3. We are able to extrapolate contours of TES resistance near the trajectory because we have precise measurements of both α_I and β_I at each of the bias points. This plot illustrates the shape of the surface $R(I,T)$ and the shape of the phase transition near the trajectory.

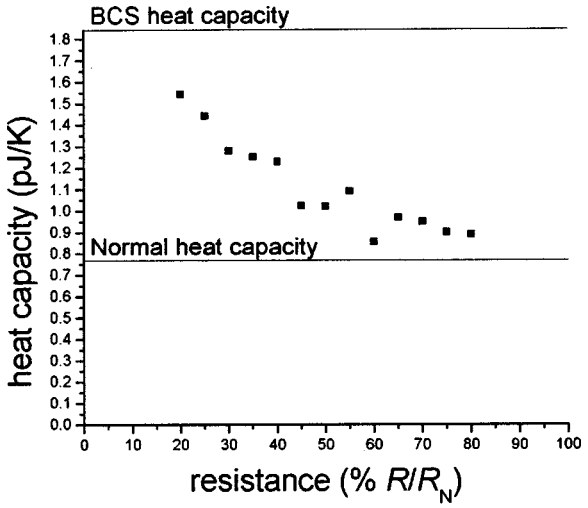

FIG. 11. Heat capacity measurements of a 500 μm square Mo/Au TES obtained through fitting the linear model to current pulses from the absorption of Al Kα x rays. These data agree with impedance measurements of the heat capacity: They show that heat capacity increases from the calculated normal state heat capacity to BCS heat capacity as the TES resistance is decreased by lowering the bias voltage.

However, pulses due the absorption of x rays in our TES calorimeters typically involve larger excursions of resistance, temperature, and current. In this case, nonlinear behavior of the calorimeter can affect the fit of the linear model to the pulses, resulting in scatter in the measurements of the heat capacity C as in Fig. 11.

The dependence of the TES resistance on current must be included in the model to fit the impedance data. In Fig. 5, we plot the best fit of the model to data (with $\beta_I = 0.852$), and the same model with $\beta_I = 0$. In a model with no current dependence, such as that presented by Mather[10] in 1982, the high frequency impedance $Z(\infty)$ equals the TES resistance R_0. Such a model without β_I cannot fit the TES impedance data because the high frequency impedance of the TES is larger than the resistance of the TES. The high frequency impedance of a calorimeter with a current dependent resistance is $Z(\infty) = R_0(1+\beta_I)$. Models in which the current dependence of the resistance is included (such as those by Mather[15] in 1984 and Lindeman[11] in 2000) fit the data well.

ACKNOWLEDGMENTS

The authors thank Simon Labov and Matthias Frank (at Lawrence Livermore National Laboratory) for their assistance with the development of the TES microcalorimeter model and formalism. The dc SQUID arrays were provided by the National Institute of Standards and Technology in Boulder, Colorado. We also thank Massimiliano Galeazzi, who suggested measuring impedance to obtain more precise measurements of the heat capacity than we had previously obtained by fitting our model to pulses. Dan McCammon, Galeazzi, and others at the University of Wisconsin, Madison

have previously measured the impedance to find heat capacity and thermal conductance in their silicon calorimeters. This work was performed while the author held a National Research Council Research Associateship Award at Goddard Space Flight Center.

[1] http://constellation.gsfc.nasa.gov
[2] F. M. Finkbeiner, R. P. Brekosky, J. A. Chervenak, E. Figueroa-Feliciano, M. J. Li, M. A. Lindeman, C. K. Stahle, C. M. Stahle, and N. Tralshawala, AIP Conf. Proc. **605,** 215 (2002).
[3] C. K. Stahle, M. A. Lindeman, E. Figueroa-Feliciano, M. J. Li, N. Tralshawala, F. M. Finkbeiner, R. P. Brekosky, and J. A. Chervenak, AIP Conf. Proc. **605,** 223 (2002).
[4] Caroline K. Stahle, Regis P. Brekosky, Enectali Figueroa-Feliciano, Fred M. Finkbeiner, John D. Gygax, Mary J. Lee, Mark A. Lindeman, F. Scott Porter, and Nilesh Tralshawala, Proc. SPIE **4140**, 367 (2000).
[5] Mark A. Lindeman, Regis P. Brekosky, Enectali Figueroa-Feliciano, Fred M. Finkbeiner, Mary Li, Caroline K. Stahle, Carl M. Stahle, and Nilesh Tralshawala, AIP Conf. Proc. **605,** 203 (2002).
[6] R. P. Welty and J. M. Martinis, IEEE Trans. Magn. **27**, 2924 (1991).
[7] M. E. Huber, P. A. Neil, R. G. Benson, D. A. Burns, A. M. Corey, C. S. Flynn, Y. Kitaygorodskaya, O. Massihzadeh, J. M. Martinis, and G. C. Hilton, IEEE Trans. Appl. Supercond. **11**, 1251 (2001).
[8] Kent D. Irwin, Ph.D. thesis, Stanford University, 1995.
[9] K. D. Irwin, G. C. Hilton, D. A. Wollman, and J. M. Martinis, Appl. Phys. Lett. **69**, 1945 (1996).
[10] John C. Mather, Appl. Opt. **21**, 1125 (1982).
[11] Mark A. Lindeman, Ph.D. thesis, University of California, Davis, 2000.
[12] Mark A. Lindeman, Regis P. Brekosky, Enectali Figueroa-Feliciano, Fred M. Finkbeiner, Mary Li, Caroline K. Stahle, Carl M. Stahle, and Nilesh Tralshawala, AIP Conf. Proc. **605,** 219 (2002).
[13] S. H. Moseley, J. C. Mather, and D. McCammon, J. Appl. Phys. **56**, 1257 (1984).
[14] Enectali Figueroa-Feliciano, Ph.D. thesis, Stanford University, 2001.
[15] John C. Mather, Appl. Opt. **23**, 3181 (1984).